The Astrophysical Journal, 803:44 (9pp), 2015 April 10 doi:10.1088/0004-637X/803/1/44

INTERNETWORK CHROMOSPHERIC BRIGHT GRAINS OBSERVED WITH IRIS AND SST

Juan Martínez-Sykora[1,2], Luc Rouppe van der Voort[3], Mats Carlsson[3], Bart De Pontieu[1,3], Tiago M. D. Pereira[3], Paul Boerner[1], Neal Hurlburt[1], Lucia Kleint[4], James Lemen[1], Ted D. Tarbell[1], Alan Title[1], Jean-Pierre Wuelser[1], Viggo H. Hansteen[3,1], Leon Golub[5], Sean McKillop[5], Kathy K. Reeves[5], Steven Saar[5], Paola Testa[5], Hui Tian[5], Sarah Jaeggli[6], and Charles Kankelborg[6]

[1] Lockheed Martin Solar and Astrophysics Laboratory, Palo Alto, CA 94304, USA; j.m.sykora@astro.uio.no
[2] Bay Area Environmental Research Institute, Sonoma, CA, USA
[3] Institute of Theoretical Astrophysics, University of Oslo, P.O. Box 1029 Blindern, NO-0315 Oslo, Norway
[4] University of Applied Sciences and Arts Northwestern Switzerland, 5210 Windisch, Switzerland
[5] Harvard-Smithsonian Center for Astrophysics, 60 Garden Street, Cambridge, MA 02138, USA
[6] Department of Physics, Montana State University, Bozeman, P.O. Box 173840, Bozeman, MT 59717, USA
Received 2014 December 20; accepted 2015 February 10; published 2015 April 13

ABSTRACT

The Interface Region Imaging Spectrograph (IRIS) reveals small-scale rapid brightenings in the form of bright grains all over coronal holes and the quiet Sun. These bright grains are seen with the IRIS 1330, 1400, and 2796 Å slit-jaw filters. We combine coordinated observations with IRIS and from the ground with the Swedish 1 m Solar Telescope (SST) which allows us to have chromospheric (Ca II 8542 Å, Ca II H 3968 Å, Hα, and Mg II k 2796 Å) and transition region (C II 1334 Å, Si IV 1403 Å) spectral imaging, and single-wavelength Stokes maps in Fe I 6302 Å at high spatial (0.″33), temporal, and spectral resolution. We conclude that the IRIS slit-jaw grains are the counterpart of so-called acoustic grains, i.e., resulting from chromospheric acoustic waves in a non-magnetic environment. We compare slit-jaw images (SJIs) with spectra from the IRIS spectrograph. We conclude that the grain intensity in the 2796 Å slit-jaw filter comes from both the Mg II k core and wings. The signal in the C II and Si IV lines is too weak to explain the presence of grains in the 1300 and 1400 Å SJIs and we conclude that the grain signal in these passbands comes mostly from the continuum. Although weak, the characteristic shock signatures of acoustic grains can often be detected in IRIS C II spectra. For some grains, a spectral signature can be found in IRIS Si IV. This suggests that upward propagating acoustic waves sometimes reach all the way up to the transition region.

Key words: line: profiles – Sun: atmosphere – Sun: chromosphere – Sun: oscillations – Sun: transition region – waves

Supporting material: animations

1. INTRODUCTION

Waves can be observed throughout all layers of the solar atmosphere. Understanding the properties of waves is important because of their impact on chromospheric and coronal heating and the solar wind. In addition, waves have the potential to serve as a diagnostic to measure magneto-thermal properties and to decide which physical processes are important in the different layers in the solar atmosphere.

In this study, we concentrate on the internetwork of the quiet Sun where observations in chromospheric spectral lines such as Ca II H 3968 Å and Ca II K 3933 Å are dominated by small grains: short-lived (100 s or less), sub-arcsecond regions with enhanced intensity (see, e.g., the extensive review by Rutten & Uitenbroek 1991). Handy et al. (1999), Rutten et al. (1999), and Tian et al. (2010), among others, show that the TRACE near-UV also nicely reveals the bright grains. These grains result from acoustic waves that propagate upward in the non-magnetic environment and turn into shocks as they reach the chromosphere (e.g., Carlsson & Stein 1992, 1994, 1997). Ca II K spectral profiles emerging from acoustic shocks, the so called K-grains, were studied under non-LTE conditions in one-dimensional (1D) hydrodynamic models by Carlsson & Stein (1992, 1997) and in three-dimensional (3D) models under LTE conditions by Wedemeyer et al. (2004).

Propagating from the upper layers of the photosphere, the acoustic waves steepen into acoustic shocks in the chromosphere due to the steep decrease in density (Carlsson & Stein 1992, 1997; Wedemeyer et al. 2004; Danilovic et al. 2014, among others).

One may expect that these grains could be traced throughout the chromosphere and transition region. Assuming that the shocks continue to travel upward, the density decrease through the chromosphere and transition region would lead to a sharpening of the shock and an increase in the shock amplitude. However, observations from the Solar Ultraviolet Measurements of Emitted Radiation (SUMER, Wilhelm et al. 1995) on board the *Solar and Heliospheric Observatory* (*SOHO*, Domingo et al. 1995) and from the Vacuum Tower Telescope (VTT, Bendlin & Volkmer 1995) indicated that the shocks that produced K-grains apparently barely have a transition region counterpart (Carlsson et al. 1997; Judge et al. 1997; Steffens et al. 1997). Carlsson et al. (1997) could trace the acoustic wave related oscillations in the UV continua and the spectral lines of neutral species, but only occasionally and faintly in spectral lines of singly ionized species (C II 1335 Å). Spectral lines from double ionized species, the "hottest" lines in their sample, did not show signs of acoustic wave related oscillations in the internetwork. Judge et al. (1997) concluded that upward-propagating acoustic shock waves do not contribute significantly to the heating of the lower transition region. The question then remains how these acoustic waves are

dissipated before they reach the transition region and to what extent they contribute to chromospheric heating in the quiet Sun.

In this paper, we focus on acoustic chromospheric waves in the quiet Sun and the coronal hole internetwork using some of the highest-resolution observations to date: in the UV from space with the Interface Region Imaging Spectrograph (IRIS, De Pontieu et al. 2014) and the strong chromospheric lines Hα and Ca II 8542 Å from the ground with the Swedish 1 m Solar Telescope (SST, Scharmer et al. 2003). These instruments provide a combination of high spatial, spectral, and temporal resolution.

The paper is laid out as follows. The data processing of the various instruments is described in Section 2. In Section 3, we follow up with the observational results which focus on (1) the properties of bright chromospheric internetwork grains (Section 3.1); (2) the origin of the emission of these grains (Section 3.2); and (3) the spectral analysis (Section 3.3). Finally, we discuss the results and conclusions in Section 4.

2. OBSERVATIONS

IRIS obtains spectra in passbands from 1332 to 1358 Å (with a spectral pixel size of 12.98 mÅ), 1389 to 1407 Å (with a spectral pixel size of 12.72 mÅ), and 2783 to 2834 Å (with a spectral pixel size of 25.46 mÅ) including bright spectral lines formed in the chromosphere (e.g., Mg II h 2803 Å and k 2796 Å), in the upper chromosphere/lower transition region (C II 1334/1335 Å), and in the transition region (e.g., Si IV 1394/1403 Å). Spectral rasters sample regions up to 130″ × 175″ at a variety of spatial samplings (from 0.″33 and up). In addition, IRIS can take slit-jaw images (SJI) with different filters that have spectral windows dominated by the emission from these spectral lines. SJI 2796 is centered on Mg II k at 2796 Å and has a 4 Å bandpass, SJI 1330 is centered at 1340 Å and has a 55 Å bandpass, and SJI 1400 is centered at 1390 Å and has a 55 Å bandpass. For more information on IRIS, we refer the reader to De Pontieu et al. (2014). We analyze both sit-and-stare, i.e, with the slit pointing at a fixed solar region and continuously tracking solar rotation, and large spatial raster IRIS observations.

The sit-and-stare observations were obtained on 2013 September 22 from 07:34:30 to 11:04:13 UT where the IRIS slit was kept at a fixed location to maximize the temporal cadence. The cadence of the spectral observations was 5 s with an exposure time of 4 s. SJI with the 1330, 1400, and 2796 Å filters were taken every 10 s. Calibrated level two data were used in our study, i.e., dark subtraction, flat field correction, and geometrical correction have been taken into account (De Pontieu et al. 2014). The target was a coronal hole at $(x, y) \sim (537'', 282'')$. For this data set, we acquired coordinated observations with the SST (Scharmer et al. 2003) on La Palma using the CRisp Imaging Spectro-Polarimeter (CRISP, Scharmer et al. 2008) and imaging in the blue beam. CRISP provides us with spectrally resolved imaging in Hα and Ca II 8542 Å, and single-wavelength Stokes I, Q, U, V images in the wing (−48 mÅ) of Fe I 6302 Å. The time range for CRISP was 08:09:00–10:10:47 UT. For the period with best seeing (08:20:39–09:08:43), we acquired upper photospheric/chromospheric images in a Ca II H filter (1.1 Å FWHM) centered on the line core and pure photospheric images from a wide-band filter (10 Å FWHM) centered on 3953.7 Å, the bump between the Ca K and H cores. The Ca II 8542 Å spectral line was sampled at 25 spectral positions within ±1200 mÅ of the core with a sampling of 100 mÅ. The Hα line was sampled at 15 spectral positions within ±1400 mÅ with a sampling of 200 mÅ. A sharp and stable time series was achieved with the aid of adaptive optics, image restoration using the Multi-Object Multi-Frame Blind Deconvolution method (van Noort et al. 2005), and time series processing of the reconstructed images that includes derotation, rigid alignment, and destretching. For the data processing, we follow the CRISP reduction pipeline (de la Cruz Rodríguez et al. 2015) which includes procedures described by de la Cruz Rodríguez et al. (2013), Henriques (2012), van Noort & Rouppe van der Voort (2008), and Shine et al. (1994).

We aligned the SST data to the IRIS observations by scaling down to the IRIS image scale (0.″16) and through cross-correlation of the SST Ca II 8542 Å wing ($\Delta\lambda = -1$ Å) and IRIS Mg II k SJI 2796 images. The accuracy of the alignment was found to be on the level of the IRIS pixel size. The overlapping field of view (FOV) between IRIS and SST was roughly 25″ × 35″.

We also make use of very large dense IRIS level two raster data with 30 s exposures taken on 2014 February 25 at 20:50:31 UT and on 2013 October 22 at 11:30:30 UT. Each of the rasters has 400 steps and scans 132″ × 175″ in three and a half hours with a spatial pixel size of 0.″16 along the slit and 0.″35 as raster step size. Both rasters were on the quiet sun, the first one centered at $(x, y) = (77'', -72'')$ and the second one at $(x, y) = (-304'', -109'')$. To allow for a reasonable 32 s cadence for the SJI, only two SJI filters were used in each raster: the 1330 and 1400 Å SJIs were used in the first raster, and the 1400 and 2796 Å SJIs used in the second raster. We analyze both rasters here in order to have observations in all three filters.

Solar Dynamic Observatory/Helioseismic and Magnetic Imager (*SDO*/HMI Scherrer et al. 2012) data have been used for the context of the same region and time such as the two deep exposure IRIS raster observations (2014 February 25 at 20:50:30 UT, and 2013 October 22 at 11:30:30 UT). We use the magnetic field along the line of sight distributed with the `ssw_jsoc_time2data.pro` and `read_sdo.pro` and the data was processed using `aia_prep.pro`.

3. RESULTS

Small-scale and dynamic bright grains dominate images and time series of the quiet Sun and coronal holes observed with the IRIS 1400, 1330, and 2796 Å SJI filters (e.g., see Figures 1, 2, and 4). The properties of these chromospheric bright grains (CBGs), the origin of their emission in these filters, and their spectral analysis are described in the following Sections 3.1–3.3, respectively.

3.1. Properties of the CBGs

We use the CRISP Fe I 6302 Å Stokes V maps to select the CBGs observed with the IRIS SJI filters that are located in internetwork regions with weak magnetic fields and to make sure that they are not related to isolated magnetic bright points or network regions (see panel (B) in Figure 1). Therefore, we do not study the isolated magnetic bright points studied by Sivaraman & Livingston (1982), Sivaraman et al. (2000), and De Wijn et al. (2008). The typical size of the CBGs is of the order of 0.″5 – 1.″5 with, in general, a round shape. Others are elongated, such as the example located at $(x, y) = (553'', 294'')$

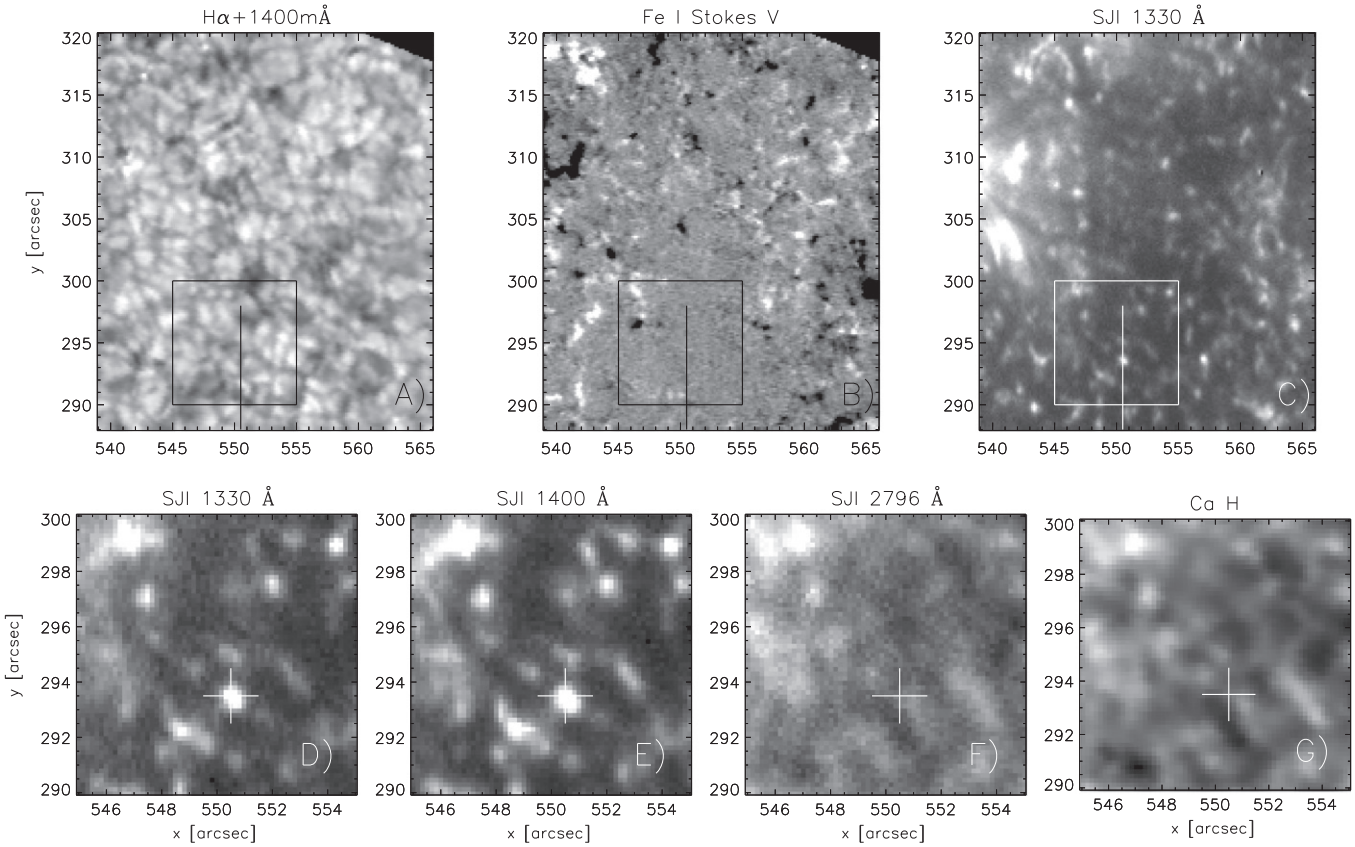

Figure 1. Chromospheric bright grains (CBGs) in an internetwork region taken 2013 September 22 at 08:28:47 UT (which corresponds to $t = 3250$ s in Figures 2 and 3) centered at $(x, y) = (537'', 282'')$. The observed region shown in the top panels is very quiet as can be inferred from the photospheric Hα far wing image at +1400 mÅ (panel (A)), and the Fe I 6302 Å Stokes V magnetogram (panel (B)). The IRIS SJI 1330 Å image (panel (C)) is dominated by small bright grains scattered over the FOV. The vertical line in the top panels marks the location of the space/time diagram in Figure 2. The rectangular box marks a region with a particularly low polarization signal that is shown at larger magnification in the panels in the bottom row. CBGs in IRIS SJI 1330 Å (panel (D)), SJI 1400 Å (panel (E)), SJI 2796 Å (panel (F)), and Ca II H (panel (G)) core maps overlap in time and space. The CBGs have a typical size of 1″ and lifetime of 1.5 minutes (see the corresponding Movie 1). The crosses in the bottom panels mark the location used for which the light curves are shown in Figure 3.

(An animation of this figure is available.)

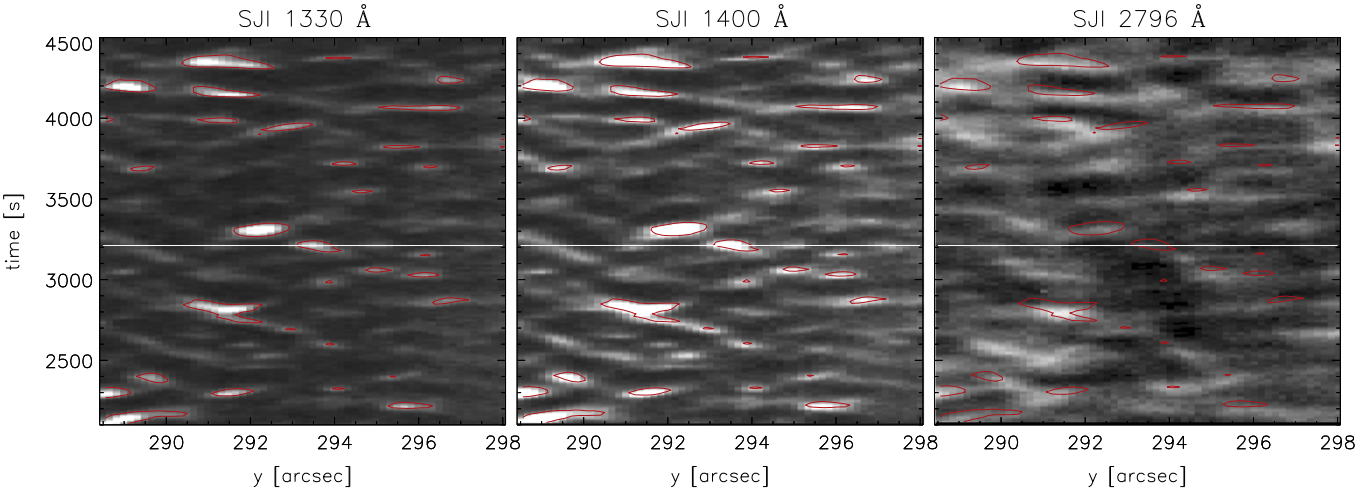

Figure 2. Internetwork space/time diagram of IRIS SJI 1330 Å (left), 1400 Å (middle), and 2796 Å (right). The red contours correspond to SJI 1330 Å. The selected region is marked in Figure 1. The white line marks the time for which images are shown in Figure 1.

(see panels (D)–(G)). The elongation can become as long as intergranular lanes (~2″). CBGs observed with SJI 1330 Å (panel (D)), and 1400 Å (panel (E)) are clearly more round than those observed with SJI 2796 Å (panel (F)) and in Ca II H (panel (G)).

The CBGs observed in each SJI channel and Ca II H correspond to the same feature, which is illustrated in Figure 1 and in Movie 1. Overlap of the CGBs can also be discerned in space and time in all three channels (see Figure 2). In addition, they show a nice correlation with the

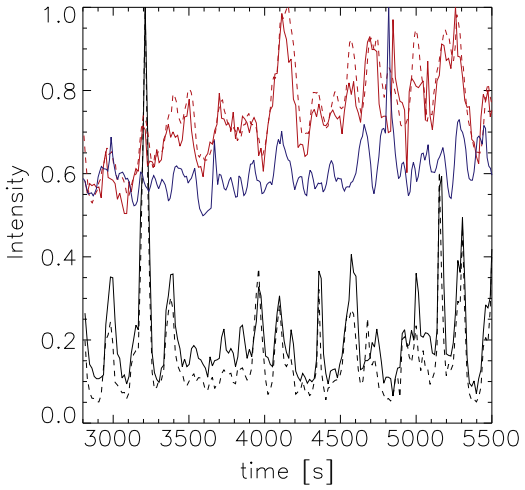

Figure 3. Light curves for a selected position in an internetwork region with very low magnetic activity (marked with the cross in the bottom panels in Figure 1): SJI 1330 Å (solid black line), 1400 Å (dashed black line), 2796 Å (solid red line) filters, and Ca II H (dashed red line) and the integrated line core of Ca II 8542 Å (solid blue line). All light curves are normalized.

Ca II 8542 Å line core intensity. The structures are highly similar between the SJI 1330 and 1400 Å filters and between SJI 2796 Å and Ca II H (see Figure 1 and Movie 1). Between these two sets of images (one set IRIS FUV SJIs and the other set the longer wavelength passbands, i.e., SJI 2796 Å and Ca II H), the brightenings seem to come from the same feature, but they show some differences in structure and brightness. Therefore, the CBG emission in the SJI 1330 and 1400 Å filters is probably from a different atmospheric region than SJI 2796 Å and Ca II H, but still from the same features (see Section 3.2). We note that there seems to be a trend in the time evolution of the CBG's emission (Figures 2 and 3) being most of the time first seen in SJI 2796 Å and with longer duration than in the FUV channels. Within the context of upward propagating waves, this can be interpreted as the signal of the SJI 2796 filter originating over a wider (and mostly deeper) height range. Note that there is not always a nice time match between SJI 2796 and SJI 1330/1400; sometimes the CBGs appear earlier, sometimes later in time. An example of this mis-match between SJI 2796 and SJI 1330/1400 is shown in Figure 3 between 4400 and 4600 s (see Section 3.3).

The light curves of the SJI CBGs and Ca II H as a function of time are shown in Figure 3. In general, CBGs show the largest variation in the 1400 Å SJI filter, then in the 1330 Å SJI filter, and the variability in the 2796 Å SJI filter and Ca II H are the lowest. As mentioned above, there is a clear similarity between the SJI 1330 and 1400 Å light curves and between SJI 2796 Å and Ca II H. Ca II 8542 Å also matches nicely with the SJI 1330 and 1400 Å light curves (e.g., $t = [8400, 8600]$s).

Finally, but not least important, bright grains move horizontally. This is seen in Figure 2 as inclined trajectories of the grains with a typical velocity of 7 km s^{-1} (see also Movie 1).

3.2. Origin of the CBGs Emission

The SJI 1330 Å filter is dominated by the C II 1334 and 1336 Å lines, the SJI 1400 Å filter by the Si IV 1394 and 1403 Å lines, and the SJI 2796 Å filter by the Mg II k 2796 Å line. Is the CBG brightening in the SJI filters coming from these dominant lines? We used rasters of long exposure observations taken with the IRIS spectrograph to address this question. Two different observations were used so that we can analyze all three IRIS SJI filters (SJI 1330 and 1400 Å for 2014 February 15, SJI 2796 and 1400 Å for 2013 October 22).

For context, we show SJI 1400 images (top panels) and the line-of-sight magnetic field maps from HMI (bottom panels) in Figure 4. The context images serve to illustrate the low level of magnetic activity and the ubiquitous presence of CBGs over the whole FOV.

The 30 s exposure spectroheliograms allow us to search for possible line emission in Mg II k, C II, and Si IV in CBGs in the IRIS SJI filter images. For this we integrated the spectral profiles as a function of wavelength and subtracted from Mg II k the wings intensity and from C II and Si IV the continuum intensity in order to construct averaged line intensity maps (see the top panels of Figure 6). The spectral windows used for integration are illustrated in Figure 5. The black profiles are averaged over the whole data set which includes network regions. Spectral profiles of one CBG are shown in blue (smoothed over three spectral pixels for C II and Si IV to reduce noise). The Mg II k wing intensity is calculated by averaging in wavelength from λ_{-1} to λ_0 and from λ_1 to λ_2. The continuum intensity for the C II and Si IV lines is averaged from λ_1 and λ_2. The averaged continuum or Mg II k wing intensities are then subtracted from the average line profile intensity (between λ_0 and λ_1). In Figure 6, such integrated intensity maps of the dominant lines from the raster are compared with the corresponding synthetic SJI raster maps (bottom panels).

The raster maps were recorded with the slit oriented in the east–west direction (along the x-axis in Figure 6) and stepping in the north–south direction (along the y-axis). Horizontal bands with black and white pixels are caused by enhanced noise from energetic particle hits on the detectors when the spacecraft passed through the Earth's radiation belts (South Atlantic Anomaly). Vertical dark lines are due to artifacts on the slit. The corresponding synthetic SJI raster maps in the bottom row are corrected for the temporal raster stepping: the maps are constructed from intensity profiles neighboring the slit taken from SJI images that match the raster spectrograms. Note, we cannot get exactly co-spatial SJI data with the raster slit.

The two Mg II k maps (left panels in Figure 6 and Movie 2) are very similar and are both dominated by CBGs and structures that appear reminiscent of reversed granulation. SUNRISE observed also similar structures in Mg II k (Danilovic et al. 2014). This shows that CBGs have a clear contribution from the Mg II k line core. Note that even though the SJI 2796 filter has rather narrow bandwidth (4 Å), there is still a significant contribution from the inner wings. For the construction of the integrated line intensity map in the top panel, the wing contribution has been subtracted and there still is a significant CBG contribution. The wing map (not shown) is also dominated by CBGs which leads to the conclusion that CBG signals in the SJI 2796 filter comes both from the Mg II k line core and inner wings and explains why the contrast in both raster maps is not identical.

The C II integrated line intensity map (top right panel of Figure 6) is rather different from the SJI 1330 map (bottom right) although close inspection reveals faint presence of some CBGs in the C II map (see right panels on Movie 2). One clear example of the latter is the selected case shown as the blue

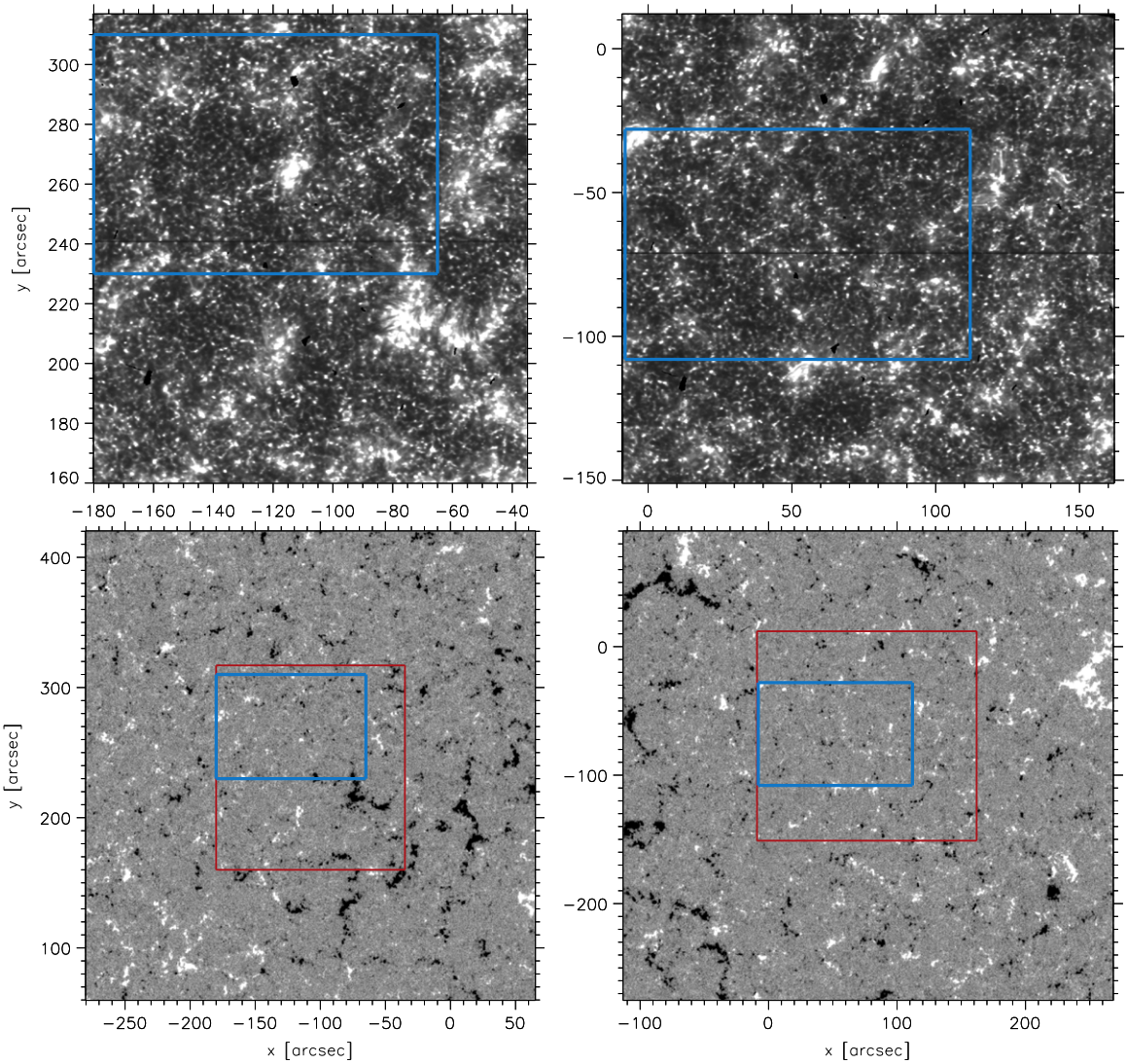

Figure 4. Context maps for the deep rasters shown in Figure 6: SJI 1400 (top panels) and HMI line-of-sight magnetograms (bottom panels). The left panels are taken on 2013 October 22 at 11:30:30 UT and the right panels on 2014 February 25 at 20:50:31 UT. The red box in the bottom panels delimits the FOV shown in the top panels and the blue boxes mark the FOV shown in Figure 6. The IRIS spectrograph slit is visible as the dark horizontal line in the middle of the SJI images (the satellite was rolled 90° with respect to solar north).

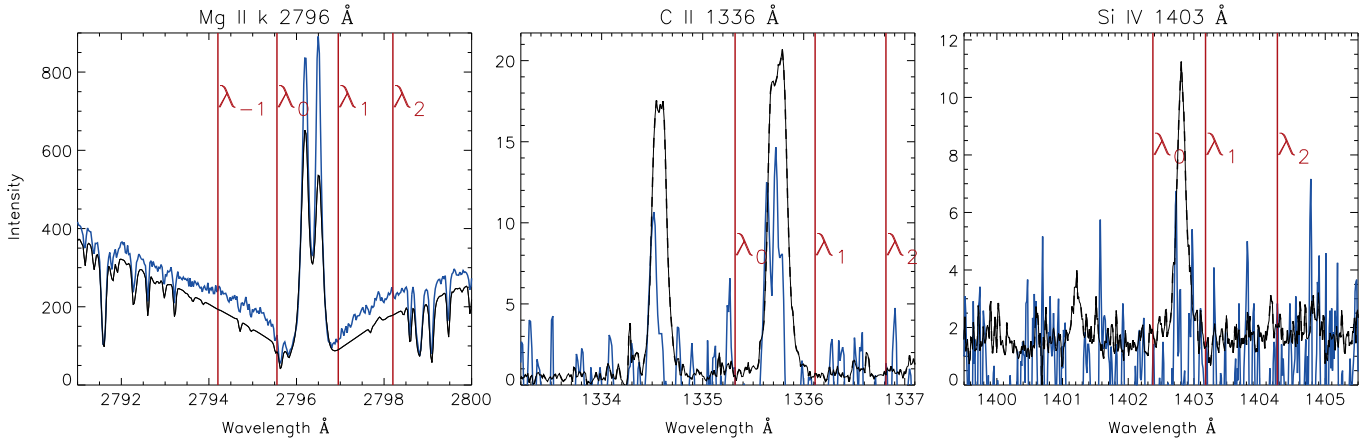

Figure 5. Observed spectral windows for the Mg II k line (left), the C II lines (middle), and Si IV (right). The black spectral profiles are spatially averaged over the full field of view of the IRIS raster of 2013 October 22 at 11:30:30 UT, including both internetwork and network regions. The blue spectral profiles are from one chromospheric bright grain (smoothed over three spectral pixels for C II and Si IV to suppress noise). The vertical red lines mark the spectral windows to construct the integrated line maps (between λ_0 and λ_1) and to estimate the wing intensity for Mg II k (between λ_{-1} and λ_0, plus between λ_1 and λ_2) and continuum intensity for C II and Si IV (between λ_1 and λ_2).

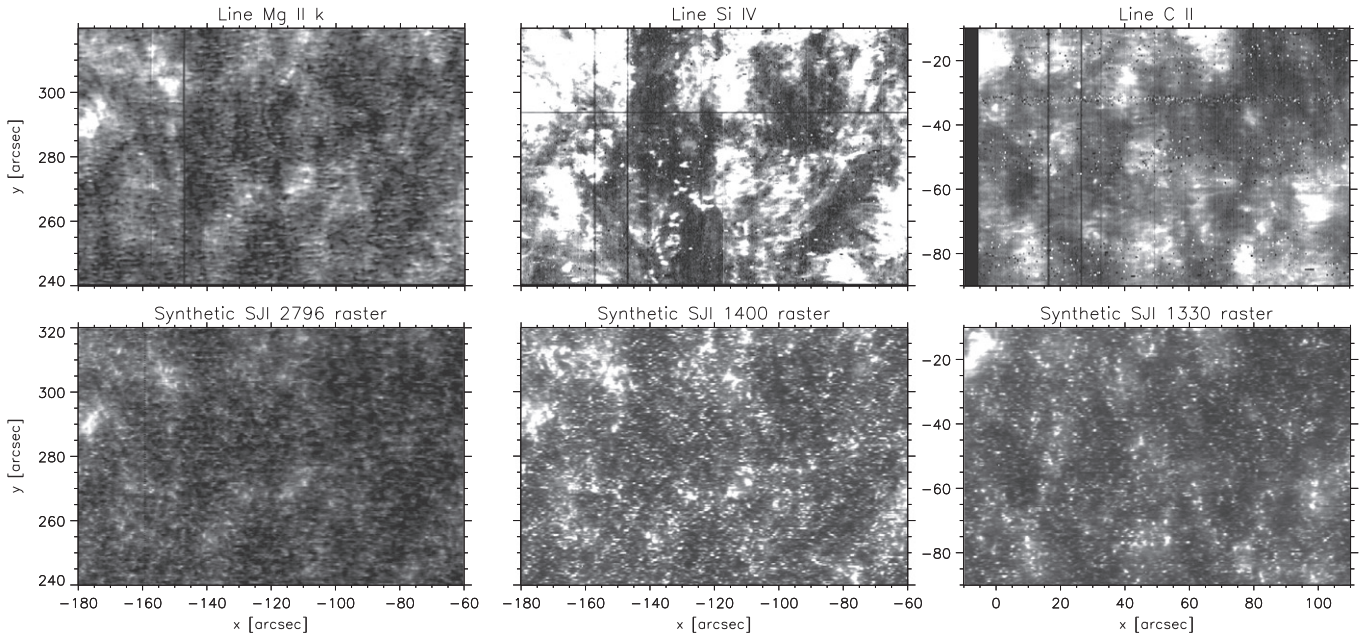

Figure 6. Top row: integrated intensity maps of the Mg II k (left panel), Si IV 1403 Å (middle panel), and C II 1336 Å (right panel) lines from 30 s exposure dense raster observations with the slit oriented aligned E–W. Bottom row: associated Mg II k (left panel), Si IV 1403 Å (middle panel), and C II 1330 Å (right panel) filter synthetic raster maps constructed from a series of SJI images with time correction to match the raster. The field of view covers a very quiet internetwork region with only a few network elements near the edges (see context images in Figure 4). The first two columns are from observations on 2013 October 22 at 11:30:30 UT, the right column is from observations on 2014 February 25 at 20:50:31 UT. The gray scale ranges through the same normalized range for each channel and is linear. See corresponding Movie 2.

(An animation of this figure is available.)

profile in Figure 5 which is a CBG with a clear signal in C II and no signal in Si IV. The Si IV 1403 Å map is filled with fibrils (middle top panel of Figure 6, studied in detail by, e.g., De Pontieu et al. 2007; Pereira et al. 2014; Tian et al. 2014) and only in a few regions one can see weak grains such as around $(x, y) = (-140'', 250'')$ and $(x, y) = (-120'', 245'')$. The fibrilar structures are mostly saturated to visualize the faint CBGs. The brightness of the few grains in Si IV and C II intensities is lower than the fibrils; therefore, the CBG's Si IV and C II emission is too weak to contribute significantly to the grain signal observed in SJI 1400 and 1330 Å (Figure 6 and Movie 2). If these spectral lines do not produce the CBG's emission in these two filters, then where does the signal come from? Presumably, the emission of CBGs in the 1400 and 1330 Å SJI filters comes from the continuum. The observed continuum from the IRIS spectrograph is very weak and often does not exceed the digitization threshold, i.e., we could not directly confirm if most of the CBGs emission in these two filters comes from the continuum by constructing integrated continuum maps like we did for the spectral lines. The continuum windows in the IRIS FUV spectrograms are simply too narrow compared to the 55 Å bandpass of the SJI filters to make a direct comparison. Consequently, we postulate that grains in SJI 1400 and 1330 Å are mostly caused by an integrated continuum over the wide filter bandpass.

By comparison with the spectrally resolved data for Hα and Ca II 8542 Å from CRISP, we can make a rough estimate of the formation height of the SJI 1400 and 1330 Å bright grains. For this, we focus on CBGs within coronal holes and quiet sun internetwork, i.e., far from photospheric magnetic bright points. We use the Fe I 6302 Å Stokes V maps to select CBGs that are in the internetwork: Figure 7 and Movie 3 show CBGs identified in SJI 1400 as red contours in different diagnostics. The black/white contours outline regions with enhanced Stokes V signal. In order to find the origin of the CBGs emission in SJI 1330 Å (top left panel), 1400 Å (top middle panel), and 2796 Å (top right panel) we compare them with Ca II H core (bottom left panel), Hα at various wavelength positions (bottom middle panel), and Ca II 8542 Å at different wavelength positions (bottom right panel) shown in Movie 3. Most of the emission seems to come from the network, but still, bright grains appear frequently all over in coronal holes and quiet sun internetwork (see Figures 1 and 4). SJI bright grains tend to be located at the outer part of dark region boundaries in Ca II H, i.e., at the bright region of the reverse granulation. Hα maps differ the most from any of the SJI filters. Only in the line core of Hα can one see a few similarities. Figure 7 and Movie 2 reveal a rather large overlap between Ca II 8542 Å, Ca II H maps, and 1400 and 1330 Å SJI filters. The best match of SJI 1330 and 1400 Å CBGs is with bright grains as seen in the line core intensity of Ca II 8542 Å (see Movie 3). Note that we have integrated the line core intensity over ± 0.1 Å with respect to the wavelength of the darkest core intensity in order to avoid cross-talk between the Doppler-shift and core intensity variations. The correlation between the Ca II 8542 Å core intensity and IRIS slitjaws is also noticeable in the lightcurves shown in Figure 3. The continuum of the SJI 1330 and 1400 Å filters is normally formed at a lower height than the core of the Ca II 8542 Å line (roughly 0.8 Mm Vernazza et al. 1981 versus 1.3 Mm Cauzzi et al. 2008). However, in a dynamic atmosphere, the intensity of the UV continua may obtain a large contribution from the shock even when the shock is significantly higher than the optical depth unity height (Carlsson & Stein 1995). This explains the similarity between the SJI 1330/1400 Å and Ca II 8542 Å core intensities.

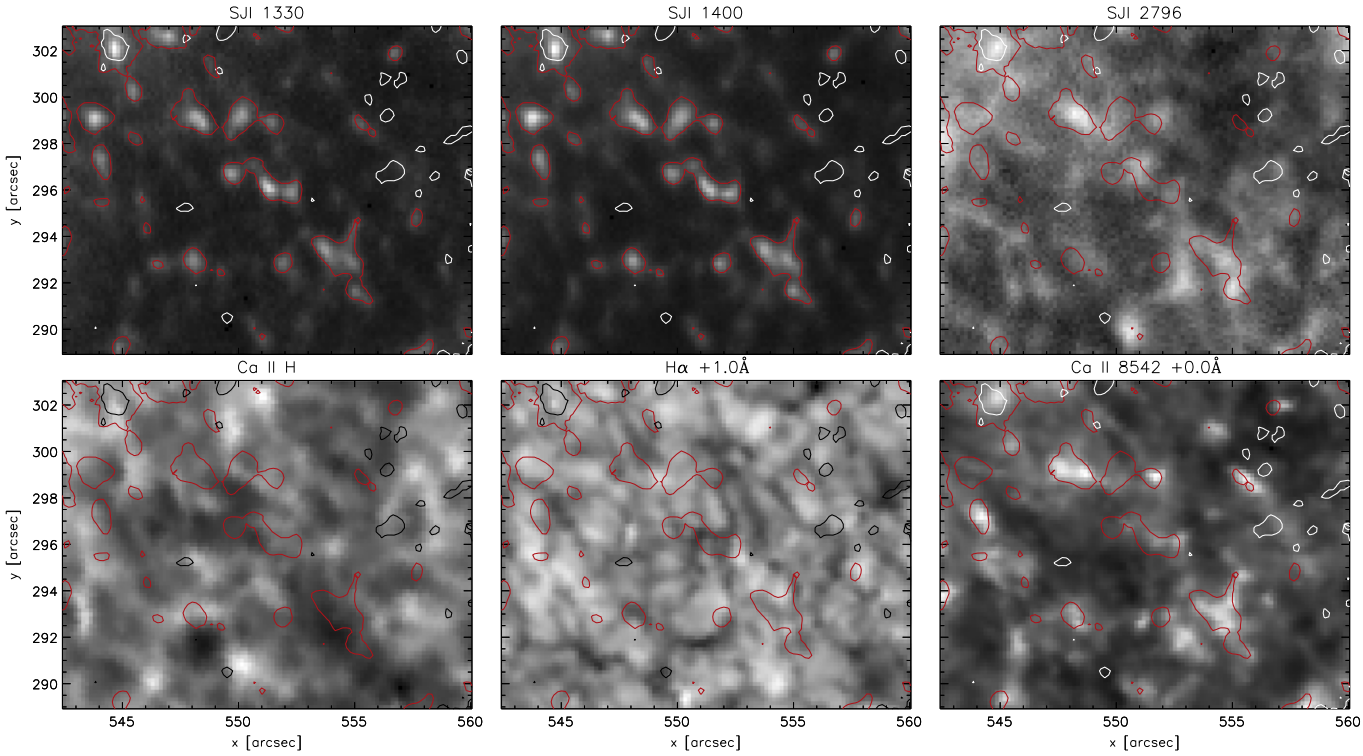

Figure 7. CBGs in UV (top row: SJI 1330, SJI 1400, and SJI 2796) and optical (bottom row: line core of Ca II H, Hα, and Ca II 8542 Å) diagnostics. Red contours outline CBGs defined in SJI 1400, black/white contours outline Stokes V signals. See corresponding Movie 3. The CBG locations match well, especially in the UV images and the Ca II 8542 line core.

(An animation of this figure is available.)

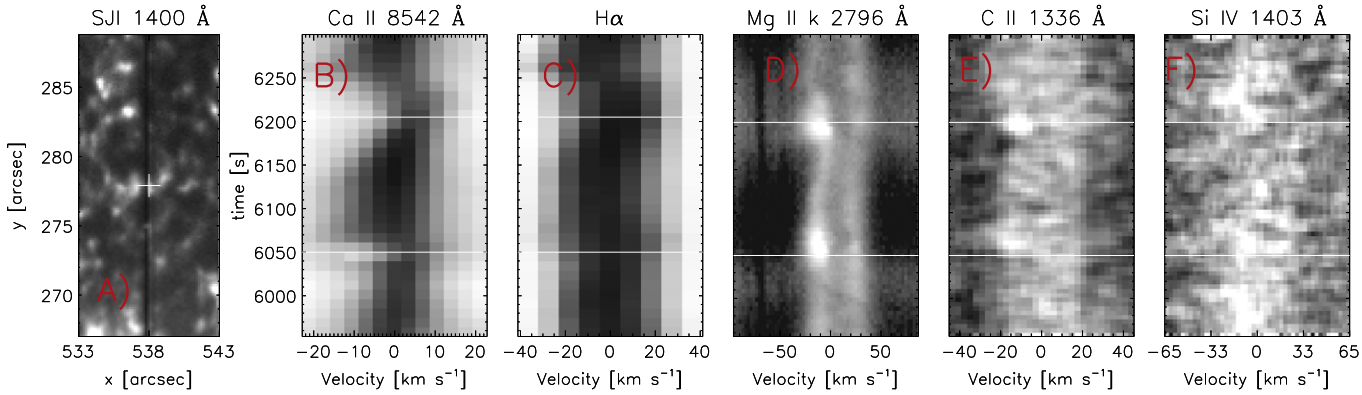

Figure 8. Spectral profiles as a function of time for Ca II 8542 Å, Hα, Mg II k, C II, and Si IV are shown, respectively, in panels (B)–(F). The context image is shown in panel (A) at time 6200 s (marked with the top horizontal white line in panels (B)–(F)) where the CBG is captured by the slit (top white cross). This CBG also shows a weak signal in C II (panel (E)) and Si IV (panel (F)). We binned the signal in C II over five spatial pixels, two spectral pixels, and two consecutive temporal snapshots (i.e., 20 spectra). For Si IV, we binned over seven spatial pixels, two spectral pixels, and two consecutive temporal snapshots (i.e., 28 spectra). The white horizontal lines are drawn to guide the eye for the time of the Ca II 8542 blue wing brightening.

3.3. Spectral Analysis

Both SST and IRIS provide spectral information as a function of time for CBGs. Figure 8 shows Ca II 8542 Å, Hα, Mg II k, C II, and Si IV (panels (B)–(F)) spectral profiles as a function of time for a number of SJI CBGs. The context SJI 1400 Å image is shown in panel (A) at time = 6200 s (marked with the upper horizontal white line in panels (B)–(F)). The λ–t plots of the chromospheric spectral lines reveal a wave pattern (panels (B)–(D)). Two nice examples of CBGs are at $t = 6050$ and 6200 s in the figure (marked with the two horizontal white lines).

At the beginning of the bright grain evolution, the core of the chromospheric lines are blueshifted up to -4 km s^{-1} for Ca II 8542 Å and Hα, and -10 km s^{-1} for Mg II k for the absorption part of the spectral line. These Doppler velocities are roughly sonic, i.e., their amplitudes in Doppler velocity shift are rather small, most likely because the centroid velocity does not capture shocks since these lines are optically thick (Carlsson & Stein 1997). Only at the moment of maximum Doppler shift, the k2v peak shows a large intensity increase in both CBGs. It is known that a shock passing through the middle chromosphere produces an increase in density and temperature leading to a large intensity increase in the peak of

Mg II k2v (Leenaarts et al. 2013a, 2013b; Pereira et al. 2013, detail the formation of the Mg II h & k lines in a simulated atmosphere) similar to the asymmetric intensity increase observed in the strong Ca II lines (panel (B); Rutten & Uitenbroek 1991). It is also interesting to see that at the later stage of the wave in Ca II 8542 Å and Hα, the blue wing shows an asymmetry with an absorption contribution shifted up to $-30\,\mathrm{km\,s^{-1}}$. As mentioned in the previous section, only some cases reveal some signal in the transition region lines, for instance the CBG example at $t = 6200$ s, weak signals of C II ($-15\,\mathrm{km\,s^{-1}}$, panel (E)) and Si IV ($-20\,\mathrm{km\,s^{-1}}$, panel (F)) can be discerned. Similarly, the other example (at $t = 6050$ s) has an increase in C II intensity with comparable Doppler shifts. The signal in Si IV is very noisy and weak in CBGs (see for instance Figures 5 and 6). Still, a weak Si IV signal around $t = 6200$ s can be discerned at $-20\,\mathrm{km\,s^{-1}}$. Therefore, the Doppler shift, as expected for an upward traveling wave into lower density regions, increases with formation height from Ca II 8542 Å ($\sim -4\,\mathrm{km\,s^{-1}}$), H$\alpha$ ($\sim -5\,\mathrm{km\,s^{-1}}$) Mg II k ($\sim -10\,\mathrm{km\,s^{-1}}$), C II ($\sim -15\,\mathrm{km\,s^{-1}}$), to Si IV ($\sim -20\,\mathrm{km\,s^{-1}}$). However, one must be really careful with interpreting the shifts in the core of Ca II 8542 Å, Hα, and Mg II k as Doppler shifts since these are optically thick.

Temporal evolution of Ca II 8542 Å, Hα, and Mg II k spectral profiles for a pixel in the internetwork in a coronal hole have a wave pattern with, sometimes, a time difference of a few seconds between each of them. For instance, the CBG at $t = 6200$ s shows the brightening in the blue wing in Ca II 8542 Å earlier than the brightening in Mg II k2v peak, whereas these two brightenings are reversed in time of appearence in the CBG at $t = 6050$ s. Going through the data (not showing everything here), we find a similar number of appearances for both cases. If we for a moment make the naive assumption of the Ca II 8542 Å brightening being formed at lower heights than Hα and even lower heights than Mg II k, then one may interpret this as one case being an upward propagating wave and the other one as a downward propagating wave. Far from this, panel (D) reveals that both CBGs come from upward propagating waves since there first appears an increased intensity in the wings of Mg II k propagating inwards toward the line core. This is a clear sign of an upward propagating wave. Once again, similar to the fact that one must be careful to interpret the line core shifts as Doppler shifts, caution must be exercised in the interpretation of the brightening at the blue side of the line profile. This brightening comes about through an interplay between a local source function maximum and the velocity gradient in optically thick line formation (for a detailed discussion, see Carlsson & Stein 1997). Therefore, normal height of formation arguments must be treated with caution—numerical simulations combined with non-LTE radiative transfer calculations giving synthetic observables may help with a more detailed interpretation.

4. DISCUSSION AND CONCLUSIONS

We analyzed bright grains observed in the internetwork of coronal holes and the quiet sun with the IRIS SJI 1330, 1400, and 2796 Å filters. CBGs have a lifetime of roughly 1.5–2 minutes in the SJI 1330, 1400 Å filters and 2.5 minutes in the SJI 2796 Å filter and Ca II H. The longer duration in the SJI 2796 Å filter is, most likely, due to the fact that this spectral passband better covers the atmospheric height range for which the CBGs give enhanced emission. The filter (4 Å passband) includes both inner wings and line core of Mg k so that this channel covers CBGs from the upper-photosphere to the chromosphere (Pereira et al. 2013). This explains why this channel shows CBGs for a longer period of time than the other two SJI channels. We find a good correlation between the light curves of the SJI 1330 and 1400 Å filters and between the SJI 2796 Å filter and Ca II H. It is clear that the CBG signal through the SJI 2796 Å filter comes from the same range of heights as Ca II H. In addition, the intensity observed in the SJI 1330 and 1400 Å filters must come from the same region. From a comparison of integrated line maps and SJI images, we conclude that CBGs in these two IRIS filters are dominated by the continuum intensity and not by the C II and Si IV emission lines in these filters. Therefore, CBGs observed with the IRIS 1330 and 1400 Å slit-jaws sample conditions between the upper photosphere and middle chromosphere; as a matter of fact, they match rather nicely with the Ca II 8542 Å line core taken with the SST. Moreover, bright grains in SJI 1400 and 1330 Å appear toward the end of the lifetime of the SJI 2796 Å features. Assuming that these events travel upwards, the signal may come from roughly the middle chromosphere since the grains in SJI 1400 and 1330 Å seem to form more or less at similar heights as the core of Mg II k.

If grains are a consequence of shocks and the density drops drastically between the chromosphere and transition region, then one may expect a greater amplitude of the shock in the transition region. Note that most of the CBGs signal in the SJI filters comes from the chromosphere and not from the transition region. Using the IRIS spectrograph, we were able to reveal that CBGs sometimes have weak and smooth emission in C II (in agreement with Carlsson et al. 1997) and in a few cases in Si IV too, i.e., such waves can reach the transition region. Their emission get blurry and extremely weak, most likely due to expansion of the shock when it travels through the chromosphere and reaches overlying loops. Further studies of CBGs simulations should seek if overlaying loops and canopy structures can lead to weak emission in transition region lines and/or stop the propagation of the shocks into the transition region. Another open question is if shocks with weak signals in the transition region can get into the corona.

For the first time we tie the same shock in Ca II 8542 Å, Hα, and Mg II k and with a weak signal in C II, and in a few cases in Si IV. In addition, we match these signatures in the various spectral profiles with CBGs in the IRIS SJI filters. Ca II 8542 Å, Hα, and Mg II k profiles reveal shock patterns with amplitudes of roughly $4\,\mathrm{km\,s^{-1}}$ for Ca II 8542 Å and Hα and $10\,\mathrm{km\,s^{-1}}$ for Mg II k and their lifetime is roughly ~1.5 minutes. C II and Si IV revealed only a weak brightening around $20\,\mathrm{km\,s^{-1}}$. However, one must be careful to interpret the line core shifts of the chromospheric lines because they are optically thick. As a matter of fact, we see that the Ca II 8542 Å brightening is sometimes produced before and other times after the intensity increase of Mg II k2v. However, in both cases, Mg II k reveals that the wave is propagating upwards since the enhancement in intensity appears first in the wings and propagates in time toward the core of the line.

We gratefully acknowledge support by NASA grants NNX11AN98G and NNM12AB40P, and NASA contracts NNM07AA01C (Hinode) and NNG09FA40C (IRIS). This work has benefited from discussions at the International Space Science Institute (ISSI) meeting on "Heating of the magnetized

chromosphere" from 2014 February 24–28 where many aspects of this paper were discussed with other colleagues. To analyze the data, we have used IDL and the Solar SoftWare library (SSW). The Swedish 1 m Solar Telescope is operated by the Institute for Solar Physics of the Royal Swedish Academy of Sciences in the Spanish Observatorio del Roque de los Muchachos of the Instituto de Astrofísica de Canarias. This research was supported by the Research Council of Norway and by the European Research Council under the European Union's Seventh Framework Programme (FP7/2007–2013)/ ERC grant agreement No. 291058. Thanks are also due to Hakon Skogsrud, Eamon Scullion, and Ada Ortiz for performing the observations at the SST.

REFERENCES

Bendlin, C., & Volkmer, R. 1995, A&AS, 112, 371
Carlsson, M., Judge, P. G., & Wilhelm, K. 1997, ApJL, 486, L63
Carlsson, M., & Stein, R. F. 1992, ApJL, 397, L59
Carlsson, M., & Stein, R. F. 1995, ApJL, 440, L29
Carlsson, M., & Stein, R. F. 1994, Radiation Shock Dynamics in the Solar Chromosphere—Results of Numerical Simulations, ed. M. Carlsson (Oslo, Norway: Institute of Theoretical Astrophysics), 47
Carlsson, M., & Stein, R. F. 1997, ApJ, 481, 500
Cauzzi, G., Reardon, K. P., Uitenbroek, H., et al. 2008, A&A, 480, 515
Danilovic, S., Hirzberger, J., Riethmüller, T. L., et al. 2014, ApJ, 784, 20
de la Cruz Rodríguez, J., Löfdahl, M., Sütterlin, P., Hillberg, T., & Rouppe van der Voort, L. 2015, A&A, 573, A40
de la Cruz Rodríguez, J., Rouppe van der Voort, L., Socas-Navarro, H., & van Noort, M. 2013, A&A, 556, A115
De Pontieu, B., Hansteen, V. H., Rouppe van der Voort, L., van Noort, M., & Carlsson, M. 2007, ApJ, 655, 624
de Pontieu, B., Title, A. M., Lemen, J. R., et al. 2014, SoPh, 289, 2733
De Wijn, A. G., Lites, B. W., Berger, T. E., et al. 2008, ApJ, 684, 1469
Domingo, V., Fleck, B., & Poland, A. I. 1995, SoPh, 162, 1
Handy, B. N., Acton, L. W., Kankelborg, C. C., et al. 1999, SoPh, 187, 229
Henriques, V. M. J. 2012, A&A, 548, A114
Judge, P., Carlsson, M., & Wilhelm, K. 1997, ApJL, 490, L195
Leenaarts, J., Pereira, T. M. D., Carlsson, M., Uitenbroek, H., & De Pontieu, B. 2013a, ApJ, 772, 89
Leenaarts, J., Pereira, T. M. D., Carlsson, M., Uitenbroek, H., & De Pontieu, B. 2013b, ApJ, 772, 90
Pereira, T. M. D., De Pontieu, B., Carlsson, M., et al. 2014, ApJL, 792, L15
Pereira, T. M. D., Leenaarts, J., De Pontieu, B., Carlsson, M., & Uitenbroek, H. 2013, ApJ, 778, 143
Rutten, R. J., de Pontieu, B., & Lites, B. 1999, in ASP Conf. Ser. 183, Internetwork Grains with TRACE, ed. T. R. Rimmele, K. S. Balasubramaniam, & R. R. Radick (San Francisco, CA: ASP), 383
Rutten, R. J., & Uitenbroek, H. 1991, SoPh, 134, 15
Scharmer, G. B., Bjelksjo, K., Korhonen, T. K., Lindberg, B., & Petterson, B. 2003, Proc. SPIE 4853, 341
Scharmer, G. B., Narayan, G., Hillberg, T., et al. 2008, ApJL, 689, L69
Scherrer, P. H., Schou, J., Bush, R. I., et al. 2012, SoPh, 275, 207
Shine, R. A., Title, A. M., Tarbell, T. D., et al. 1994, ApJ, 430, 413
Sivaraman, K. R., Gupta, S. S., Livingston, W. C., et al. 2000, A&A, 363, 279
Sivaraman, K. R., & Livingston, W. C. 1982, SoPh, 80, 227
Steffens, S., Deubner, F.-L., Fleck, B., & Wilhelm, K. 1997, ESA Special Publication Vol. 404, Tracing CA K Grains Through the Chromosphere into the Transition Region, ed. A. Wilson, 685
Tian, H., DeLuca, E. E., Cranmer, S. R., et al. 2014, Sci, 346, 1255711
Tian, H., Potts, H. E., Marsch, E., Attie, R., & He, J.-S. 2010, A&A, 519, A58
van Noort, M., Rouppe van der Voort, L., & Löfdahl, M. G. 2005, SoPh, 228, 191
van Noort, M. J., & Rouppe van der Voort, L. H. M. 2008, A&A, 489, 429
Vernazza, J. E., Avrett, E. H., & Loeser, R. 1981, ApJS, 45, 635
Wedemeyer, S., Freytag, B., Steffen, M., Ludwig, H.-G., & Holweger, H. 2004, A&A, 414, 1121
Wilhelm, K., Curdt, W., Marsch, E., et al. 1995, SoPh, 162, 189